Tibial-fibular geometry and density variations associated with elevated bone strain and sex disparities in young active adults

Olivia L. Bruce*[a,b,c], Michael Baggaley[b,c], Arash Khassetarash[b,c], Ifaz T. Haider[b,c], W. Brent Edwards[a,b,c]

[a]Biomedical Engineering Graduate Program, 2500 University Drive NW, University of Calgary, Calgary, AB, CA, T2N 1N4
[b]Human Performance Laboratory, Faculty of Kinesiology, 2500 University Drive NW, University of Calgary, Calgary, AB, CA, T2N 1N4
[c]McCaig Institute for Bone and Joint Health, 3280 Hospital Dr NW, University of Calgary, Calgary, AB, CA, T2N 4Z6

Author emails:
Olivia L Bruce: olivia.bruce@ucalgary.ca
Michael Baggaley: michael.baggaley1@ucalgary.ca
Arash Khassetarash: a.khassetarash@ucalgary.ca
Ifaz T. Haider: ifaz.haider@ucalgary.ca
W. Brent Edwards: wbedward@ucalgary.ca

Corresponding Author:
Olivia L. Bruce
KNB 414, 2500 University Drive NW
Calgary AB, CA T2N 1N4
olivia.bruce@ucalgary.ca

This is an Accepted Manuscript of an article published by Elsevier in Bone on 16 May 2022, available online: https://doi.org/10.1016/j.bone.2022.116443

Abstract

Tibial stress fracture is a common injury in runners and military personnel. Elevated bone strain is believed to be associated with the development of stress fractures and is influenced by bone geometry and density. The purpose of this study was to characterize tibial-fibular geometry and density variations in young active adults, and to quantify the influence of these variations on finite element-predicted bone strain. A statistical appearance model characterising tibial-fibular geometry and density was developed from computed tomography scans of 48 young physically active adults. The model was perturbed ± 1 and 2 standard deviations along each of the first five principal components to create finite element models. Average male and female finite element models, controlled for scale, were also generated. Muscle and joint forces in running, calculated using inverse dynamics-based static optimization, were applied to the finite element models. The resulting 95th percentile pressure-modified von Mises strain (peak strain) and strained volume (volume of elements above 4000 με) were quantified. Geometry and density variations described by principal components resulted in up to 12.0% differences in peak strain and 95.4% differences in strained volume when compared to the average tibia-fibula model. The average female illustrated 5.5% and 41.3% larger peak strain and strained volume, respectively, when compared to the average male, suggesting that sexual dimorphism in bone geometry may indeed contribute to greater stress fracture risk in females. Our findings identified important features in subject-specific geometry and density associated with elevated bone strain that may have implications for stress fracture risk.

Keywords: statistical appearance model, finite element analysis, lower extremity, morphology, stress fracture

1 Introduction

Stress fracture is a common injury in runners and military recruits [1–3]. Stress fractures frequently occur at the tibia and females are at greater risk of fracture than males [1–3]. Mechanical fatigue, a phenomenon whereby submaximal repetitive loading leads to the accumulation of microdamage, has been associated with the development of stress fractures [4]. It is important to note that the rate of damage accumulation is strongly related to bone strain magnitude [5,6].

Bone geometry and density are two factors that influence bone strain magnitude. It has been hypothesized that differences in transverse cross-sectional size, cortical thickness, and condyle size between males and females contribute to the greater risk of stress fracture in females when compared to males [7–9]. In current literature, characterization of geometry, density, and estimates of bone strength within and between sex and injury status groups has largely relied on simple measures such as cortical area, cortical thickness, section modulus, polar strength-strain index, and bone mineral content measured at transverse cross-sections. [1,7,10]. Bone strain is a complex function of bone geometry and density distribution, and can be directly estimated using subject-specific finite element models [11]. However, as a numerical technique, it can be difficult to isolate the contributions of different model parameters and understand their relative impact on bone strain using finite element models alone.

This limitation could be overcome using statistical shape models (SSMs), which characterize geometry variation, and statistical appearance models (SAMs), which characterize bone geometry and density variations within a population. SSMs have been used to describe geometry variations in a variety of bones [12–16], characterize sexual dimorphism [8,9,13], and to explore the influence of geometry variations on spine and knee kinematics and joint contact mechanics [17–19]. SAMs have been developed for bones including the scapula, lumbar vertebrae, femur, and tibia [20–25]. Importantly, SAMs in combination with finite element analysis have enabled population-level investigations of knee and hip implant performance [24,25], proximal femur strength in a sideways fall [23], and vertebral stiffness [21]. The influence of tibia and fibula geometry and density variations on bone strain has yet to be investigated.

The purpose of this study was to characterize tibial-fibular geometry and density variations using a SAM and to quantify the influence of these variations on finite element-predicted bone strain in young active adults. We expected that transverse cross-sectional dimensions and cortical thickness would demonstrate the largest influence on bone strain after controlling for scale and that sex-related geometry and density variations would result in higher bone strain in the average female when compared to the average male.

2 Material and Methods

2.1 Statistical Appearance Model

A statistical appearance model was constructed using computed tomography (CT) scans of the left tibia and fibula (GE Discovery scanner, General Electric Medical System, Milwaukee, WI; acquisition settings: 120 kVp, 200 mA, in-plane resolution of 0.48 x 0.48 mm, slice thickness of 0.625 mm) obtained from forty-eight healthy adults (20 females and 28 males, age = 18-32 years, height = 1.49-1.87 m, mass = 48.3-86.0 kg). Age, height, and mass for males and females are presented in Table 1. Participants were recreationally active at least three times per week and had no musculoskeletal injuries that limited physical activity within the three months prior to scanning. All participants provided written, informed consent. Study protocol was approved by the university's Conjoint Health Research Ethics Board.

The tibia and fibula were semi-automatically segmented in the Mimics Innovation Suite (v21, Materialise, Leuven, Belgium) and triangular periosteal surface meshes were generated.

Reference four-node tetrahedral volume meshes were created from average tibia and fibula geometries, obtained from a previously described SSM based on a subset of the data used in the present study [13]. The reference tibia and fibula meshes contained 270 002 and 41 077 elements, respectively. Surface node correspondence between the reference meshes and participant geometries were established using the Coherent Point Drift algorithm [26]. Displacements between corresponding surface nodes were calculated and used as boundary conditions to morph the reference mesh to match each participant's surface geometry in Abaqus (v.2019, Dassault Systèmes Simulia Corp.; Providence, USA). The resulting meshes were then overlaid onto the participant's CT data. A hydroxyapatite calibration phantom (QRM GmbH; Moehrendorf, Germany) was used to identify a linear relationship between Hounsfield units in the CT image and equivalent bone mineral density (ρ_{HU}) for each participant. Each element was assigned a density value based on a volume-weighted average of the underlying voxels.

The resulting meshes were aligned to the reference mesh using the Procrustes algorithm, preserving scale. Principal components analysis (PCA) was applied to construct the SAM as outlined by Cootes and Taylor (2004): PCA was applied to the nodes to obtain a statistical shape model and to the density values to obtain a statistical intensity model. To account for correlations between shape and density, a further PCA was applied to a combined matrix containing shape and intensity parameters, weighted to normalize the total variance in each set, to obtain a SAM.

2.2 SAM Perturbations

The first five principal components, cumulatively accounting for 70.5% of the total variance in the model, were evaluated. The SAM was perturbed along each principal component by ± 1 and 2 standard deviations from the mean. Average principal component scores for males and females were calculated. The first principal component described isotropic scaling and related geometry and density variations, and was strongly correlated with height (r^2=0.83). Meshes representing the average male and average female geometry and density distribution, controlled for scaling and related variations, were created by perturbing all principal components except the first by their respective average scores. Meshes isolating geometry and density variation for the average male and female were generated for a secondary analysis.

2.3 Finite Element Models

Following perturbations, mesh elements were converted to ten-node tetrahedral elements. Element densities were discretized into bins, where the width of each bin was 0.01 g/cm^3 ρ_{HU}. Bin centers were used as the density value for each element. Orthotropic linear-elastic material properties were assigned to each element. The elastic modulus of bone in the axial direction was calculated as a function of element apparent bone mineral density ($\rho_{app} = \rho_{HU}/0.626$) [28]:

$$E_3 = 6570 \cdot \rho_{app}^{1.37} \quad (1)$$

The other constants were obtained assuming constant anisotropy: $E_1 = 0.574 \cdot E_3$, $E_2 = 0.577 \cdot E_3$, $G_{12} = 0.195 \cdot E_3$, $G_{23} = 0.265 \cdot E_3$, $G_{31} = 0.216 \cdot E_3$, $\nu_{12} = 0.427$, $\nu_{23} = 0.234$, $\nu_{31} = 0.405$, where subscripts 1-3 denote the medial-lateral, anterior-posterior, and axial directions, respectively [29]. This definition of material properties has demonstrated excellent agreement between cadaveric experimental measurements and finite element predictions of bone strain and fracture strength at the tibia [30,31].

A preliminary mesh convergence analysis (Supplementary Figure S6) was performed using the participant model with the largest volume. Increasing the number of elements by ~100% (tibia and fibula combined) from 132 740 and 20 241 elements to 270 002 and 41 077 elements changed 95th percentile pressure-modified von Mises strain by less than 4% and strained volume by less than 2%, suggesting the mesh was adequately converged. We conservatively selected the finer mesh, as the added computational time was negligible.

2.3 Finite Element Boundary Constraints

Boundary constraints were similar to previous work from our group, with pinned constraints at the knee and ankle and complex proximal tibia-fibula joint constraints [32]. One point at the middle of the tibial plateau was fully constrained. Surface nodes on the tibial plateau within one centimeter of the fixed point in the axial direction were kinematically coupled to rotate about the fixed point. One point on the medial condyle was fixed in the anterior-posterior direction. The ankle center of rotation was estimated as the midpoint between the malleoli and used for the application of the joint contact force. This point was constrained in the anterior-posterior and medial-lateral directions. The ankle center of rotation was coupled to surface nodes near the tibia-talus and fibula-talus interfaces, such that the coupled nodes remained free to rotate about the ankle center of rotation. The distal tibia-fibula joint was modeled with surface-based tied constraints. At the proximal tibia-fibula joint, spring elements with stiffness of 133 N/mm and 109 N/mm were used to model the anterior and posterior ligaments, respectively [33]. Nodes at the articulating surface of the proximal tibia-fibula joint were tied to prevent motion in the direction normal to the joint surface.

2.4 Finite Element Loads

Lower limb joint contact force and muscle forces were calculated based on motion capture and force data from one female participant (age = 24 years, mass = 59 kg, height = 170 cm). The participant ran at 3.3 m/s on an instrumented treadmill (Bertec, Columbus, OH) while motion and force data were collected at 200 Hz and 1000 Hz, respectively, using an eight-camera Vicon Nexus system (v. 1.8.4, Vicon Motion Systems Ltd, Oxford, UK). An inverse dynamics-based static optimization routine, detailed in our previous work, was used to calculate lower extremity muscle and joint contact forces [32]. Briefly, a musculoskeletal model of the pelvis and lower limb containing fourty-five muscles [34] was scaled to the participant's segment lengths and body mass. Muscle forces were computed such that the sum of muscle moments at each joint was equal to the net joint moment computed from inverse dynamics. The following moments were used as constraints in the optimization: flexion-extension and abduction-adduction moments at the hip, flexion-extension moment at the knee, flexion-extension moment at the ankle, and the pronation-supination sub-talar moment. The optimization minimized the sum of muscle stresses squared. Ankle joint contact force and muscle forces at the time of peak resultant ankle joint contact force were scaled to the SAM average finite element model by mass (i.e., $F_{FE} = F_{participant}*(m_{average}/m_{participant})$). The same joint contact and muscle forces were applied to all models. Ankle joint contact force was applied at the ankle center of rotation. Insertion points of seventeen muscles attaching to the tibia or fibula (Supplemental Table S1) and the patellar ligament were identified by aligning the MSK model geometry and the SAM average finite element mesh using an iterative closest points algorithm and mapping each muscle point to the nearest surface node. A concentrated force was applied at each attachment point (Supplemental Table S1). A residual moment term about the sagittal and axial axes that accounts for other sources of torque (e.g., bi-articulating muscles such as the medial and lateral gastrocnemius) about the ankle was calculated for each perturbed geometry and applied at the ankle center of rotation [32].

2.5 Outcome Measures and Comparisons

Finite element models were solved in Abaqus (v.2019, Dassault Systèmes Simulia Corp.; Providence, USA). Custom Matlab (r2019a, Mathworks, Natick, MA) scripts were used to calculate pressure-modified von Mises equivalent strain, which is a modification of the von Mises strain criterion that has previously been shown to predict failure in quasi-brittle materials that demonstrate compression-tension strength asymmetry [35,36]. Analysis was limited to elements containing bone (element density values ≥ 0.5 g/cm^3) in the tibial diaphysis, defined as 20-80% of the length of the tibia [37]. The bone density threshold sensitivity was tested in the average model, and the average male and female models. Peak strain changed by less than 2.4% when thresholds of 0.5 and 1.0 g/cm^3 were used. Strained volume changed by less than 0.7% and did not affect male vs. female comparisons. We conservatively selected the lower threshold. Elements within a 1.0 cm radius of the soleus force application and a 0.5 cm radius of other muscle force application points, including transcortical elements, were removed from the analysis due to artefactually high strains (over 10 000 με). The large force applied at the attachment point for the soleus necessitated a larger radius to remove all elements with artefactually high strains. Over 98% of the elements containing bone in the tibial diaphysis remained for analysis after artefacts were removed. The 95th percentile (peak) strain and strained volume, defined as the sum of the volume of elements experiencing strain greater than or equal to 4000 με, were quantified for each model. We previously demonstrated that strained volume, with a threshold of 4000 με, was a strong predictor of fatigue life for whole rabbit tibiae in uniaxial and biaxial (compression and torsion) modes of loading [36]. At the material level, O'Brien et al. [38] observed rapid microdamage accumulation and subsequent fracture in cyclically-loaded cortical bone at a stress range of 80 MPa, which would correspond to 4000 με for an assumed elastic modulus of 20 GPa; samples loaded at lower stress ranges accumulated damage but did not fracture [38]. Absolute and percentage differences in peak strain and strained volume between perturbed models and the average model were calculated. These measures were also compared between average male and female models.

2.6 Statistical Analysis

In addition to qualitative assessments of differences between average male and female geometry and density generated from the SAM, t-tests were performed to compare principal component scores between females and males. According to Shapiro-Wilk and Levene's tests, principal component scores for male and female groups were normally distributed and had equal variances. A Sidak correction for multiple comparisons was applied such that the family-wise error rate was 0.05. Pearson product-moment correlations between scores of the first five principal components and age were also evaluated. Statistical tests were performed in SPSS (v27.0, IBM Corp., Armonk, NY).

3 Results

The first principal component, dominated by isotropic scaling, explained half (49.7%) of the total variance in the SAM. The first five principal components accounted for 70.5% of the total cumulative variance. The variance explained by the principal components are displayed in Figure 1. Geometry and density variations described by the first five principal components were independent of age ($p \geq 0.310$).

3.1 PC Perturbations

The first five principal components described tibial geometry and density variations including: isotropic scaling, axial length, cross-sectional size and geometry, curvature, and regional variations in cortical thickness and density (Table 2). The fibula varied to a lesser degree, typically displaying corresponding variations in dimensions and cortical density. Visualizations of geometry and density variations for each principal component are provided in supplementary Figures S1-S5. Perturbations of ± 1 standard deviation along these principal components resulted in 2.0-5.7% differences in peak strain and 11.5-44.6% differences in strained volume when compared to the average model (Table 2). Perturbations of ± 2 standard deviations along these principal components resulted in 3.9-12.0% differences in peak strain and 20.8-95.4% differences in strained volume when compared to the average model (Table 2).

Perturbing principal components 1, 2, and 5 resulted in the largest changes in peak strain and strained volume. The first principal component was dominated by isotropic scaling. Lower density at the endocortical surface corresponded with increased size. Increasing size by one standard deviation reduced peak strain and strained volume by 5.3% and 38.7%, respectively. The second principal component explained 10.6% of the total variance and described variations in tibia and fibula length, tibial curvature, and cortical thickness (Figure 2). A longer, straighter tibia with increased cortical thickness reduced peak strain and strained volume (perturbing by plus one standard deviation = 5.3% and 36.5% reduction in peak strain and strained volume, respectively) when compared to the average model (Figure 3). The fifth principal component explained 2.8% of total variance, describing changes in diaphysis cross-sectional size and geometry, and variation in density distribution. Increased cross-sectional size, corresponding with decreased cortical density in the anterior diaphysis and regional variations in cortical thickness, resulted in 4.0% lower peak strain and 29.1% smaller strained volume when compared to the average model.

3.2 Sexual Dimorphism

The female tibia was narrower along both anterior-posterior and medial-lateral axes and had smaller condyles. Cortical density was greater and cortical thickness in the distal ¼ of the diaphysis was smaller in the average female when compared to the average male (Figure 4). Scores for the third principal component were different between males and females ($p < 0.001$), where females had more positive scores. Principal component three illustrated similar geometry and density variations (Table 2, Supplemental Figure S3) to the observed variations between sexes. These differences resulted in 5.5% (198 $\mu\varepsilon$) higher peak strain and 41.3% (830 mm^3) higher strained volume in the average female when compared to the average male. When isolated, geometry differences resulted in 9.7% (345 με) higher peak strain and 99.5% (1678 mm^3) larger strained volume in the average female. In contrast, density differences alone resulted in 3.9% (146 με) lower peak strain and 30.6% (832 mm^3) smaller strained volume in the average female when compared to the average male.

4 Discussion

The aims of this study were to characterize tibial-fibular geometry and density variations and to quantify the influence of these variations on finite element-predicted bone strain in young active adults. Finite element-predicted bone strain was sensitive to geometry and density variations present in a young active adult population. Isotropic scaling, tibial curvature, cortical thickness, and diaphyseal dimensions in the transverse plane had the largest effects on bone strain. Sex differences in geometry were subtle yet resulted in greater bone strain in the average female than the average male when controlled for scale.

The average female model illustrated 5.5% greater 95^{th} percentile pressure-modified von Mises strain and 41.3% greater strained volume than the average male model when controlled for scaling and related variations. At the material level, strain magnitude is associated with fatigue life and the accumulation of microdamage, where higher strain results in greater damage accumulation and a shorter fatigue life [5,6]. Strained volume examines the entire strain distribution and captures the amount of bone experiencing strain above a specific threshold; in theory, a larger volume experiencing high strain has a greater probability of loading a site of localized microstructural weakness, which accelerates fatigue failure [39]. Indeed, uniaxial and biaxial mechanical tests of whole rabbit tibiae revealed strong relationships (r^2 = 0.73 and 0.59, respectively) between pressure-modified von Mises-based strained volume and fatigue life, where greater strained volume was associated with fewer loading cycles to fracture [36]. Furthermore, our finite element results are in line with clinical data. The largest area of strained volume and the highest strains, in all models, occurred on the posterior surface of the tibial diaphysis, consistent with Kijowski et al.'s [40] observations of the most frequent tibial stress fracture location. Thus, the fact that the average female illustrated greater peak strain and strained volume suggests that sexual dimorphism in the tibia and fibula, independent of applied load and scale, may indeed contribute to the greater risk of stress fracture observed in females when compared to males in a young physically active population [1–3].

The larger strains and strained volume observed in the average female when compared to the average male were explained by geometric rather than density variations. The average female tibia was smaller in the transverse plane when compared to the average male tibia; cortical area and second moment of area (i.e., resistance to bending) were also smaller through the diaphysis, leading to higher strain. In contrast, cortical density in the diaphysis was slightly greater (up to approximately 0.05 g/cm^3 greater) in the average female when compared to the average male, leading to lower strain. Specifically, when isolated, density variations resulted in 3.9% smaller peak strain and 30.6% smaller strained volume. However, the small increase in cortical density was not sufficient to offset the effects of reduced transverse cross-sectional size.

As expected, finite element-predicted strain was sensitive to scaling, geometry, and density variations among young active adults. Isotropic scaling, tibia and fibula axial length, tibial curvature, cortical thickness, and transverse cross-sectional size were the most prominent variations characterized by the SAM and resulted in substantial differences in bone strain when perturbed by ± 2 standard deviations. Increases in isotropic scaling, cortical thickness, and transverse cross-sectional dimensions are associated with increased cortical area, second moment of area, and polar moment of area, which result in reduced stresses and strains in response to axial, bending, and torsional loads. An increase in axial length would increase the moment arm of forces applied at the joints relative to the middle of the diaphysis and would result in a greater bending moment and higher strain. However, the expected effect of length on strain was not observed when evaluating the influence of the second principal component due to the greater and opposing influence of concomitant increases in cortical thickness and reduced sagittal plane curvature. In long bones, less curvature decreases bending resulting from axial loads, leading to smaller peak stresses and strains [41].

Our findings highlight the importance of obtaining subject-specific geometry and density for finite element simulations when comparing bone strain between individuals or groups, supporting previous work comparing generic and subject-specific modelling approaches [11]. When clinical computed tomography scans of the tibia and fibula are not available, statistical appearance models may serve as a tool to estimate subject-specific geometry and density from more accessible imaging methods and/or anatomical measures. For example, Väänänen et al. [42] reconstructed 3-dimensional proximal femur geometry and density from 2-dimensional clinical dual-energy x-ray absorptiometry (DXA) images using a SAM. The mean point to surface and volumetric bone mineral density errors were 1.41 mm and 0.19 g/cm^3, respectively, and this resulted in a strong correlation (r^2 = 0.85) between finite element predictions from DXA- and computed tomography-based models. Perhaps a similar approach could be developed to generate subject-specific finite element models of the tibia and fibula based on DXA, peripheral computed tomography, and/or skin-based markers. We found that tibia sagittal-plane curvature, diaphysis cortical thickness, and diaphysis transverse cross-sectional dimensions had the greatest influence on tibial bone strain. As such, obtaining measures of these factors from less intensive imaging methods may be most important for SAM-based reconstruction to minimize bone strain inaccuracies due to geometry or density prediction errors.

A limitation of our analysis was that we only modeled a single loading configuration. We chose to apply the same joint contact and muscle forces to all models to isolate the effects of geometry and density perturbations. However, contact force magnitude and direction, and the distribution of muscle forces may vary between individuals, sexes, running conditions, and other movements. For example, Meardon et al. (2021) observed smaller axial force, larger medial-lateral force, and smaller anterior-posterior bending moment at the tibia in females when compared to males during running. These factors would interact with bone geometry to determine the strain environment of the tibia and fibula. To examine the sensitivity of our results for sexual dimorphism to the applied loads, we performed a post-hoc sensitivity analysis where loads calculated based on data from a male (age = 36, height = 1.73 m, mass = 76.8 kg, running speed = 3.3 m/s; see Supplemental Table S2 for muscle and ankle contact forces) were applied to the average male and female models. Our interpretations did not change; peak strain and strained volume were greater (by 161 $\mu\varepsilon$ and 419 mm^3) in the average female when compared to the average male, controlled for scale and applied load. Still, future work evaluating the interaction between sex differences in loads and bone morphology is warranted. A second limitation of our analysis was that the training set used to build the SAM in our study was composed of only young physically active adults. The inclusion criteria for our training set limits the applicability of our SAM to other populations (e.g., clinical, pediatric, or geriatric); however, young active adults are perhaps the most studied population in biomechanics and running research.

5 Conclusions

Principal components characterising tibial curvature, cortical thickness, and cross-sectional dimensions had the greatest influence on bone strain. On average, females illustrated narrower tibiae when controlled for scale, resulting in larger strains when compared to the average male. Our findings identify key morphological parameters associated with elevated bone strain that may have implications for stress fracture risk.

6 Acknowledgements

This work was funded in part by the Natural Sciences and Engineering Research Council of Canada (RGPIN 01029-2015, 02404-2021 and CGS D – 534891 - 2019) and the NSERC CREATE Wearable Technology Research and Collaboration training program.

References

[1] F. Cosman, J. Ruffing, M. Zion, J. Uhorchak, S. Ralston, S. Tendy, F.E.A. McGuigan, R. Lindsay, J. Nieves, Determinants of stress fracture risk in United States Military Academy cadets, Bone. 55 (2013) 359–366. https://doi.org/10.1016/j.bone.2013.04.011.

[2] J.R. Kardouni, C.J. McKinnon, K.M. Taylor, J.M. Hughes, Timing of Stress Fractures in Soldiers During the First 6 Career Months: A Retrospective Cohort Study, J. Athl. Train. 56 (2021) 1278–1284. https://doi.org/10.4085/1062-6050-0380.19.

[3] K.H. Rizzone, K.E. Ackerman, K.G. Roos, T.P. Dompier, Z.Y. Kerr, The epidemiology of stress fractures in collegiate student-athletes, 2004-2005 through 2013-2014 academic years, J. Athl. Train. 52 (2017) 966–975. https://doi.org/10.4085/1062-6050-52.8.01.

[4] D. Burr, C. Milgrom, R. Boyd, W. Higgins, G. Robin, E. Radin, Experimental stress fractures of the tibia. Biological and mechanical aetiology in rabbits, J. Bone Joint Surg. Br. 72-B (1990) 370–375. https://doi.org/10.1302/0301-620X.72B3.2341429.

[5] D.R. Carter, W.E. Caler, D.M. Spengler, V.H. Frankel, Fatigue behavior of adult cortical bone: the influence of mean strain and strain range, Acta Orthop. 52 (1981) 481-490. https://doi.org/10.3109/17453678108992136.

[6] C.A. Pattin, W.E. Caler, D.R. Carter, Cyclic mechanical property degradation during fatigue loading of cortical bone, J. Biomech. 29 (1996) 69-79. https://doi.org/10.1016/0021-9290(94)00156-1.

[7] J.W. Nieves, C. Formica, J. Ruffing, M. Zion, P. Garrett, R. Lindsay, F. Cosman, Males have larger skeletal size and bone mass than females, despite comparable body size, J. Bone Miner. Res. 20 (2005) 529–535. https://doi.org/10.1359/JBMR.041005.

[8] E.A. Audenaert, C. Pattyn, G. Steenackers, J. De Roeck, D. Vandermeulen, P. Claes, Statistical Shape Modeling of Skeletal Anatomy for Sex Discrimination: Their Training Size, Sexual Dimorphism, and Asymmetry, Front. Bioeng. Biotechnol. 7 (2019) 1–11. https://doi.org/10.3389/fbioe.2019.00302.

[9] H. Brzobohatá, V. Krajíèek, Z. Horák, J. Velemínská, Sexual dimorphism of the human tibia through time: Insights into shape variation using a surface-based approach, PLoS One. 11 (2016) 1–21. https://doi.org/10.1371/journal.pone.0166461.

[10] K.L. Popp, A.C. Frye, S.D. Stovitz, J.M. Hughes, Bone geometry and lower extremity bone stress injuries in male runners, J. Sci. Med. Sport. 23 (2020) 145–150. https://doi.org/10.1016/j.jsams.2019.09.009.

[11] C. Xu, J. Reifman, M. Baggaley, W.B. Edwards, G. Unnikrishnan, Individual Differences in Women during Walking Affect Tibial Response to Load Carriage: The Importance of Individualized Musculoskeletal Finite-Element Models, IEEE Trans. Biomed. Eng. 67 (2020) 545-555. https://doi.org/10.1109/TBME.2019.2917415.

[12] T.M. Grant, L.E. Diamond, C. Pizzolato, B.A. Killen, D. Devaprakash, L. Kelly, J.N. Maharaj, D.J. Saxby, Development and validation of statistical shape models of the primary functional bone segments of the foot, PeerJ. 2020 (2020) 1–19. https://doi.org/10.7717/peerj.8397.

[13] O.L. Bruce, M. Baggaley, L. Welte, M.J. Rainbow, W.B. Edwards, A statistical shape model of the tibia-fibula complex: sexual dimorphism and effects of age on reconstruction accuracy from anatomical landmarks, Comput. Methods Biomech. Biomed. Engin. (2021) 1–12. https://doi.org/10.1080/10255842.2021.1985111.

[14] J. Zhang, D. Malcolm, J. Hislop-Jambrich, C.D.L. Thomas, P.M.F. Nielsen, An anatomical region-based statistical shape model of the human femur, Comput. Methods Biomech. Biomed. Eng. Imaging Vis. 2 (2014) 176–185. https://doi.org/10.1080/21681163.2013.878668.

[15] W.S. Burton, I. Sintini, J.M. Chavarria, J.R. Brownhill, P.J. Laz, Assessment of scapular morphology and bone quality with statistical models, Comput. Methods Biomech. Biomed. Engin. 22 (2019) 341–351. https://doi.org/10.1080/10255842.2018.1556260.

[16] I. Sintini, W.S. Burton, P. Sade, J.M. Chavarria, P.J. Laz, Investigating gender and ethnicity differences in proximal humeral morphology using a statistical shape model, J. Orthop. Res. 36 (2018) 3043–3052. https://doi.org/10.1002/jor.24070.

[17] J.Q. Campbell, A.J. Petrella, Automated finite element modeling of the lumbar spine: Using a statistical shape model to generate a virtual population of models, J. Biomech. 49 (2016) 2593–2599. https://doi.org/10.1016/j.jbiomech.2016.05.013.

[18] A.L. Clouthier, C.R. Smith, M.F. Vignos, D.G. Thelen, K.J. Deluzio, M.J. Rainbow, The effect of articular geometry features identified using statistical shape modelling on knee

biomechanics, Med. Eng. Phys. 66 (2019) 47-55. https://doi.org/10.1016/j.medengphy.2019.02.009.

[19] A.L. Clouthier, D. Borschneck, C.R. Smith, M.F. Vignos, D.G. Thelen, K.J. Deluzio, M.J. Rainbow, Influence of Articular Geometry and Tibial Tubercle Location on Patellofemoral Kinematics and Contact Mechanics, J. Appl. Biomech. 38 (2022) 58–66. https://doi.org/10.1123/jab.2021-0162.

[20] I. Sintini, Statistical Shape and Intensity Modeling of the Shoulder, University of Denver, 2017. https://digitalcommons.du.edu/etd/1478.

[21] G.A. Day, A.C. Jones, R.K. Wilcox, Using Statistical Shape and Appearance Modelling to characterise the 3D shape and material properties of human lumbar vertebrae: A proof of concept study, J. Mech. Behav. Biomed. Mater. 126 (2022) 105047. https://doi.org/10.1016/j.jmbbm.2021.105047.

[22] M.T. Bah, J. Shi, M. Browne, Y. Suchier, F. Lefebvre, P. Young, L. King, D.G. Dunlop, M.O. Heller, Exploring inter-subject anatomic variability using a population of patient-specific femurs and a statistical shape and intensity model, Med. Eng. Phys. 37 (2015) 995–1007. https://doi.org/10.1016/j.medengphy.2015.08.004.

[23] D.P. Nicolella, T.L. Bredbenner, Development of a parametric finite element model of the proximal femur using statistical shape and density modelling, Comput. Methods Biomech. Biomed. Engin. 15 (2012) 101–110. https://doi.org/10.1080/10255842.2010.515984.

[24] R. Bryan, P.B. Nair, M. Taylor, Influence of femur size and morphology on load transfer in the resurfaced femoral head: A large scale, multi-subject finite element study, J. Biomech. 45 (2012) 1952–1958. https://doi.org/10.1016/j.jbiomech.2012.05.015.

[25] F. Galloway, M. Kahnt, H. Ramm, P. Worsley, S. Zachow, P. Nair, M. Taylor, A large

scale finite element study of a cementless osseointegrated tibial tray, J. Biomech. 46 (2013) 1900–1906. https://doi.org/10.1016/j.jbiomech.2013.04.021.

[26] A. Myronenko, X. Song, Point set registration: Coherent point drifts, IEEE Trans. Pattern Anal. Mach. Intell. 32 (2010) 2262–2275. https://doi.org/10.1109/TPAMI.2010.46.

[27] T.F. Cootes, C.J. Taylor, Statistical Models of Appearance for Computer Vision, 2004.

[28] M. Dalstra, R. Huiskes, A. Odgaard, L. van Erning, Mechanical and textural properties of pelvic trabecular bone, J. Biomech. 26 (1993) 523-535. https://doi.org/10.1016/0021-9290(93)90014-6.

[29] J.Y. Rho, An ultrasonic method for measuring the elastic properties of human tibial cortical and cancellous bone, Ultrasonics. 34 (1996) 777-783. https://doi.org/10.1016/S0041-624X(96)00078-9.

[30] H.A. Gray, F. Taddei, A.B. Zavatsky, L. Cristofolini, H.S. Gill, Experimental validation of a finite element model of a human cadaveric tibia, J. Biomech. Eng. 130 (2008) 1–9. https://doi.org/10.1115/1.2913335.

[31] W.B. Edwards, T.J. Schnitzer, K.L. Troy, Torsional stiffness and strength of the proximal tibia are better predicted by finite element models than DXA or QCT, J. Biomech. 46 (2013) 1655–1662. https://doi.org/10.1016/j.jbiomech.2013.04.016.

[32] I.T. Haider, M. Baggaley, W. Brent Edwards, Subject-Specific Finite Element Models of the Tibia with Realistic Boundary Conditions Predict Bending Deformations Consistent with in Vivo Measurement, J. Biomech. Eng. 142 (2020) 1–10. https://doi.org/10.1115/1.4044034.

[33] D.C. Marchetti, G. Moatshe, B.M. Phelps, K.D. Dahl, M.B. Ferrari, J. Chahla, T.L. Turnbull, R.F. LaPrade, The proximal tibiofibular joint: A biomechanical analysis of the

anterior and posterior ligamentous complexes, Am. J. Sports Med. 45 (2017) 1888–1892. https://doi.org/10.1177/0363546517697288.

[34] E.M. Arnold, S.R. Ward, R.L. Lieber, S.L. Delp, A model of the lower limb for analysis of human movement, Ann. Biomed. Eng. 38 (2010) 269-279. https://doi.org/10.1007/s10439-009-9852-5.

[35] J.H.P. de Vree, W.A.M. Brekelmans, M.A.J. van Gils, Comparison of nonlocal approaches in continuum damage mechanics, Comput. Struct. 55 (1995) 581–588. https://doi.org/10.1016/0045-7949(94)00501-S.

[36] I.T. Haider, M. Lee, R. Page, D. Smith, W.B. Edwards, Mechanical fatigue of whole rabbit-tibiae under combined compression-torsional loading is better explained by strained volume than peak strain magnitude, J. Biomech. 122 (2021) 110434. https://doi.org/10.1016/j.jbiomech.2021.110434.

[37] W.B. Edwards, N. Simonian, K.L. Troy, T.J. Schnitzer, Reduction in Torsional Stiffness and Strength at the Proximal Tibia as a Function of Time since Spinal Cord Injury, J. Bone Miner. Res. 30 (2015) 1422–1430. https://doi.org/10.1002/jbmr.2474.

[38] F.J. O'Brien, D.A. Hardiman, J.G. Hazenberg, M. V. Mercy, S. Mohsin, D. Taylor, T.C. Lee, The behaviour of microcracks in compact bone, Eur. J. Morphol. 42 (2005) 71–79. https://doi.org/10.1080/09243860500096131.

[39] D. Taylor, Fatigue of bone and bones: An analysis based on stressed volume, J. Orthop. Res. 16 (1998) 163–169. https://doi.org/10.1002/jor.1100160203.

[40] R. Kijowski, J. Choi, K. Shinki, A.M. Del Rio, A. De Smet, Validation of MRI classification system for tibial stress injuries, Am. J. Roentgenol. 198 (2012) 878–884. https://doi.org/10.2214/AJR.11.6826.

[41] J.E.A. Bertram, A.A. Biewener, Bone curvature: Sacrificing strength for load predictability?, J. Theor. Biol. 131 (1988) 75–92. https://doi.org/10.1016/S0022-5193(88)80122-X.

[42] S.P. Väänänen, L. Grassi, G. Flivik, J.S. Jurvelin, H. Isaksson, Generation of 3D shape, density, cortical thickness and finite element mesh of proximal femur from a DXA image, Med. Image Anal. 24 (2015) 125–134. https://doi.org/10.1016/j.media.2015.06.001.

[43] S.A. Meardon, T.R. Derrick, J.D. Willson, M. Baggaley, C.R. Steinbaker, M. Marshall, R.W. Willy, Peak and Per-Step Tibial Bone Stress During Walking and Running in Female and Male Recreational Runners, Am. J. Sports Med. 49 (2021) 2227–2237. https://doi.org/10.1177/03635465211014854.

Table 1: Mean (standard deviation) participant age, height, and body mass of females and males included in the SAM.

Sex	n	Age (years)	Height (m)	Mass (kg)
F	20	19.9 (1.3)	1.65 (0.08)	60.1 (5.8)
M	28	22.4 (4.4)	1.76 (0.07)	71.5 (7.2)
p-value		0.006	<0.001	<0.001

Table 2: Geometry and density variations described by the first five principal components and their influence on 95th percentile pressure modified von Mises strain (peak ε) and strained volume (ε_{vol}) compared to the average model. Data are presented as absolute difference (percent difference).

Principal Component		**Perturbation (σ)** -2	-1	1	2	**Geometry and density variation in positive direction**
1	Peak ε (με)	446 (12.0)	205 (5.5)	-197 (-5.3)	-380 (-10.2)	Increased size Decreased density at the endocortical surface
	ε_{vol} (mm^3)	1395 (59.1)	793 (33.6)	-914 (-38.7)	-1726 (-73.2)	
2	Peak ε (με)	428 (11.5)	212 (5.7)	-195 (-5.3)	-375 (-10.1)	Longer tibia and fibula Less curvature in sagittal plane Increased density at the endocortical surface
	ε_{vol} (mm^3)	2250 (95.4)	1052 (44.6)	-861 (-36.5)	-1491 (-63.2)	
3	Peak ε (με)	-160 (-4.3)	-81 (-2.2)	75 (2.0)	146 (3.9)	Decreased cross-sectional size in proximal 2/3 of tibia Smaller proximal tibial condyles More triangular cross-section at mid-diaphysis Increased density in middle 1/3 and decreased density in proximal and distal 1/3 near the endocortical surface
	ε_{vol} (mm^3)	-616 (-26.1)	-294 (-12.5)	272 (11.5)	491 (20.8)	
4	Peak ε (με)	207 (5.6)	103 (2.8)	-100 (-2.7)	-198 (-5.3)	Larger tibia and fibula cross-sectional size Increased density in distal half, decreased density in proximal half at the endocortical surface
	ε_{vol} (mm^3)	916 (38.9)	456 (19.3)	-471 (-20.0)	-928 (-39.3)	
5	Peak ε (με)	330 (8.9)	159 (4.3)	-150 (-4.0)	-291 (-7.8)	Larger tibia and fibula cross-sectional size, especially along the A/P axis Regional variations in cortical thickness Decreased cortical density in anterior diaphysis
	ε_{vol} (mm^3)	1568 (66.5)	751 (31.9)	-686 (-29.1)	-1308 (-55.5)	

Figure 1: Percent variation (solid line) and cumulative variation (dashed line) captured by principal components of the SAM.

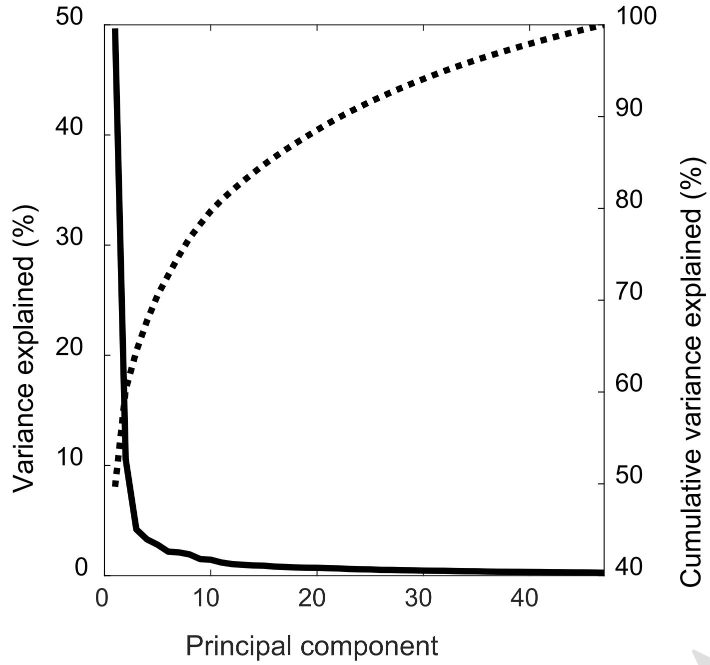

Figure 2: Geometry and density variations characterised by the second principal component. (A) Surface geometry of the tibia and fibula perturbed by +2 standard deviations (SD) (purple) and the average geometries (grey). (B) Frontal (left) and sagittal (right) cross-sections of the tibia illustrating differences in internal density distribution between +2 SD and average, where red indicates greater density in the model perturbed by +2 SD. (C) Axial cross-sections of the tibial diaphysis at 50% of total axial length.

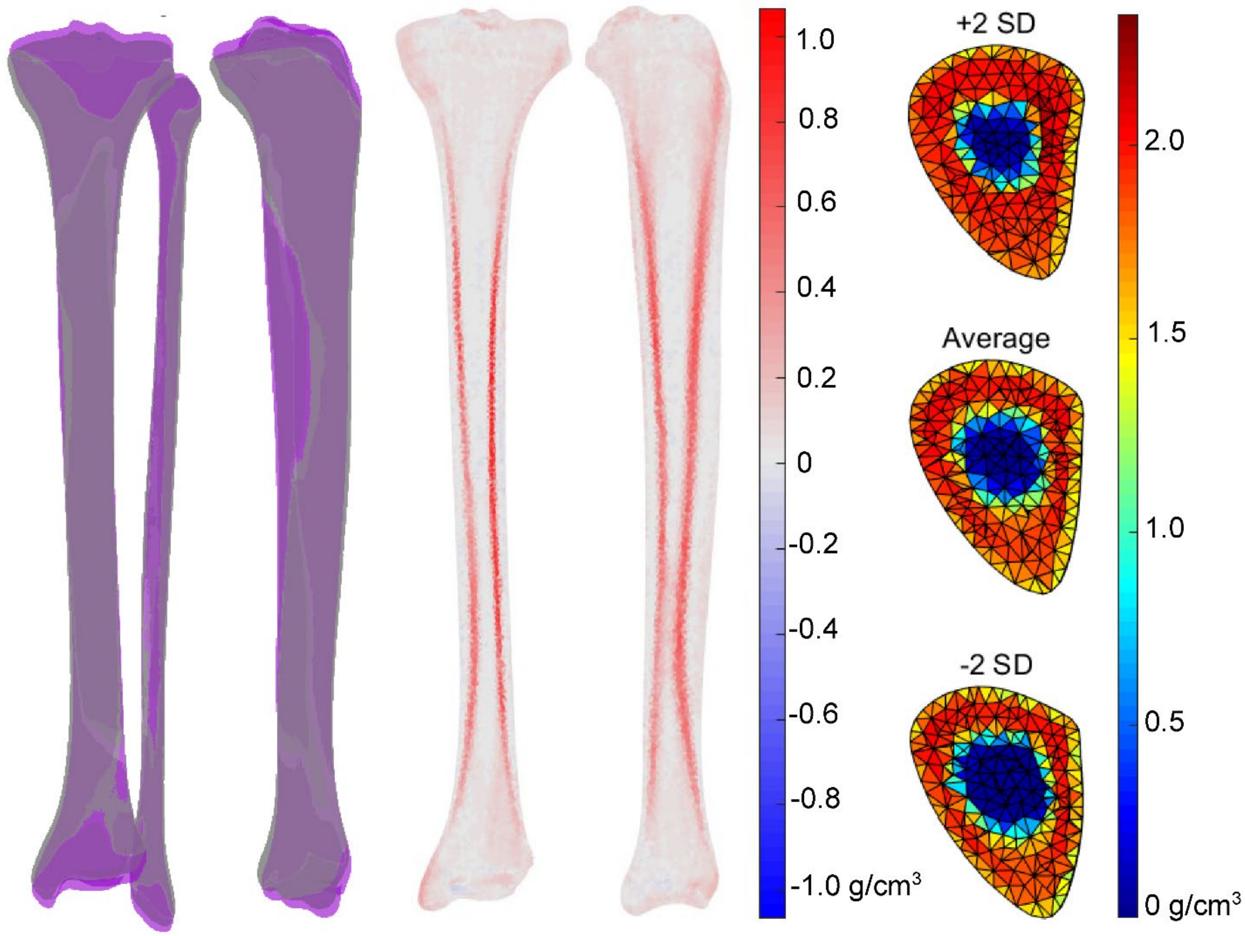

Figure 3: Pressure-modified von Mises strain distribution across the posterior surface of the tibial diaphysis for perturbations of ± 2 standard deviations (SD) along the second principal component

compared to the average. Elements coloured black (≥ 4000 με) contributed to the strained volume measure.

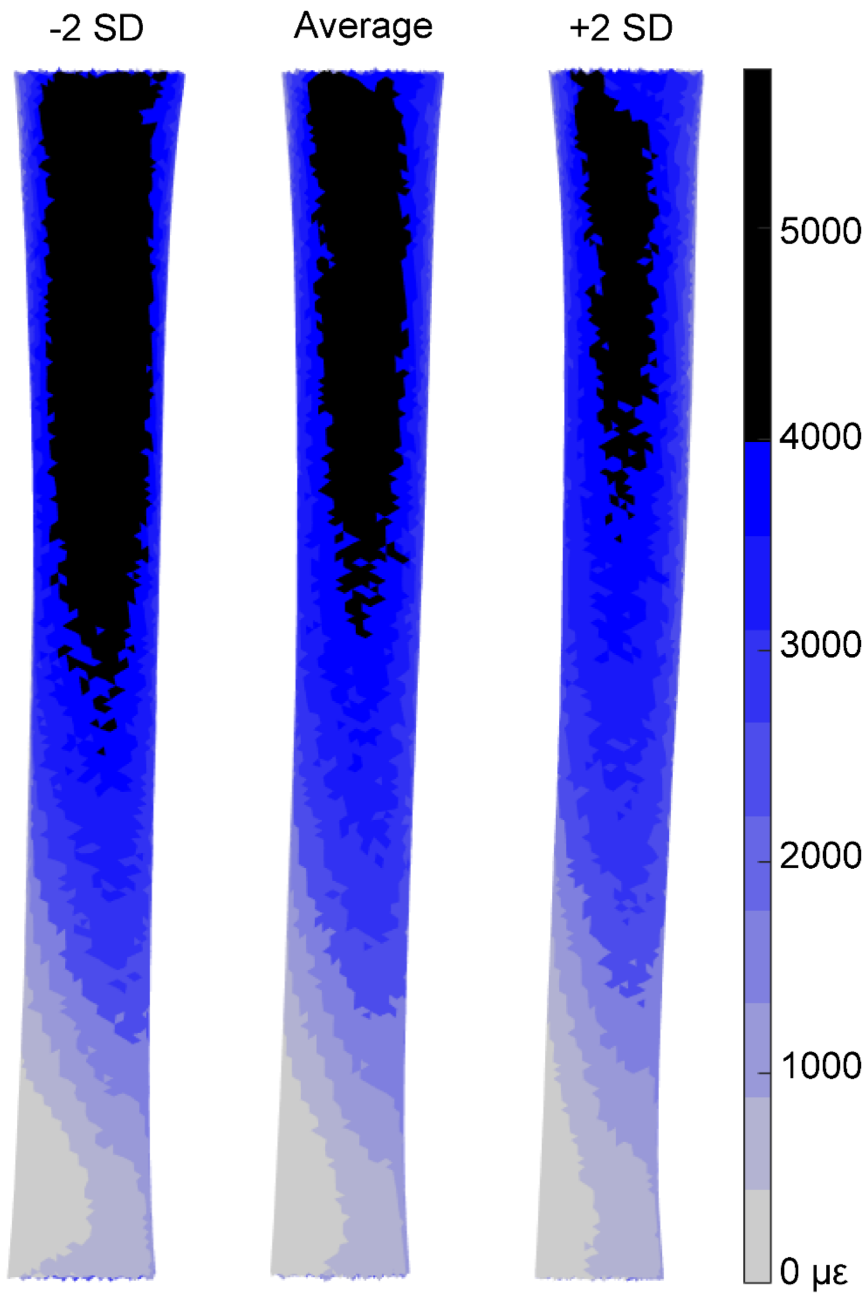

Figure 4: Comparisons between the average female and male tibia and fibula, controlled for scaling. (A) Average female (red) and male (blue) periosteal geometry. (B) Sagittal cross-section of the tibia displaying differences in density between the average female and average male, controlled for bone size.

Red indicates higher density in the female model. (C) pressure-modified von Mises strain distribution across the posterior surface of the tibial diaphysis. Elements coloured black (≥ 4000 με) contributed to the strained volume measure.

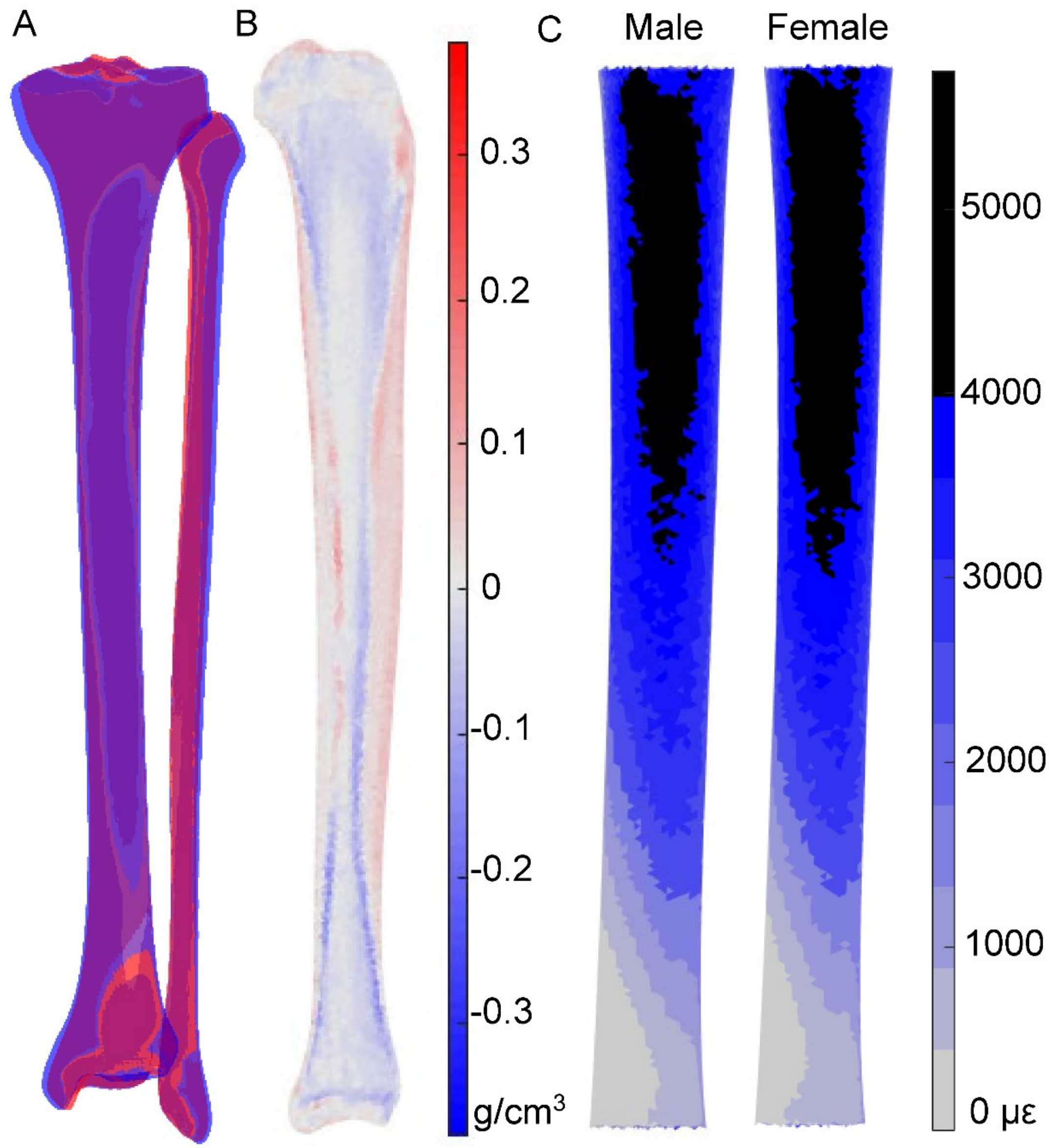

Supplemental Tables and Figures

Figure S1: Geometry and density variations characterised by the first principal component. (A) Surface geometry of the tibia and fibula perturbed by +2 standard deviations (SD) (purple) and the average geometries (grey). (B) Frontal (left) and sagittal (right) cross-sections of the tibia illustrating differences in internal density distribution between +2 SD and average, where red indicates greater density in the model perturbed by +2 SD. (C) Axial cross-sections of the tibial diaphysis at 50% of total axial length.

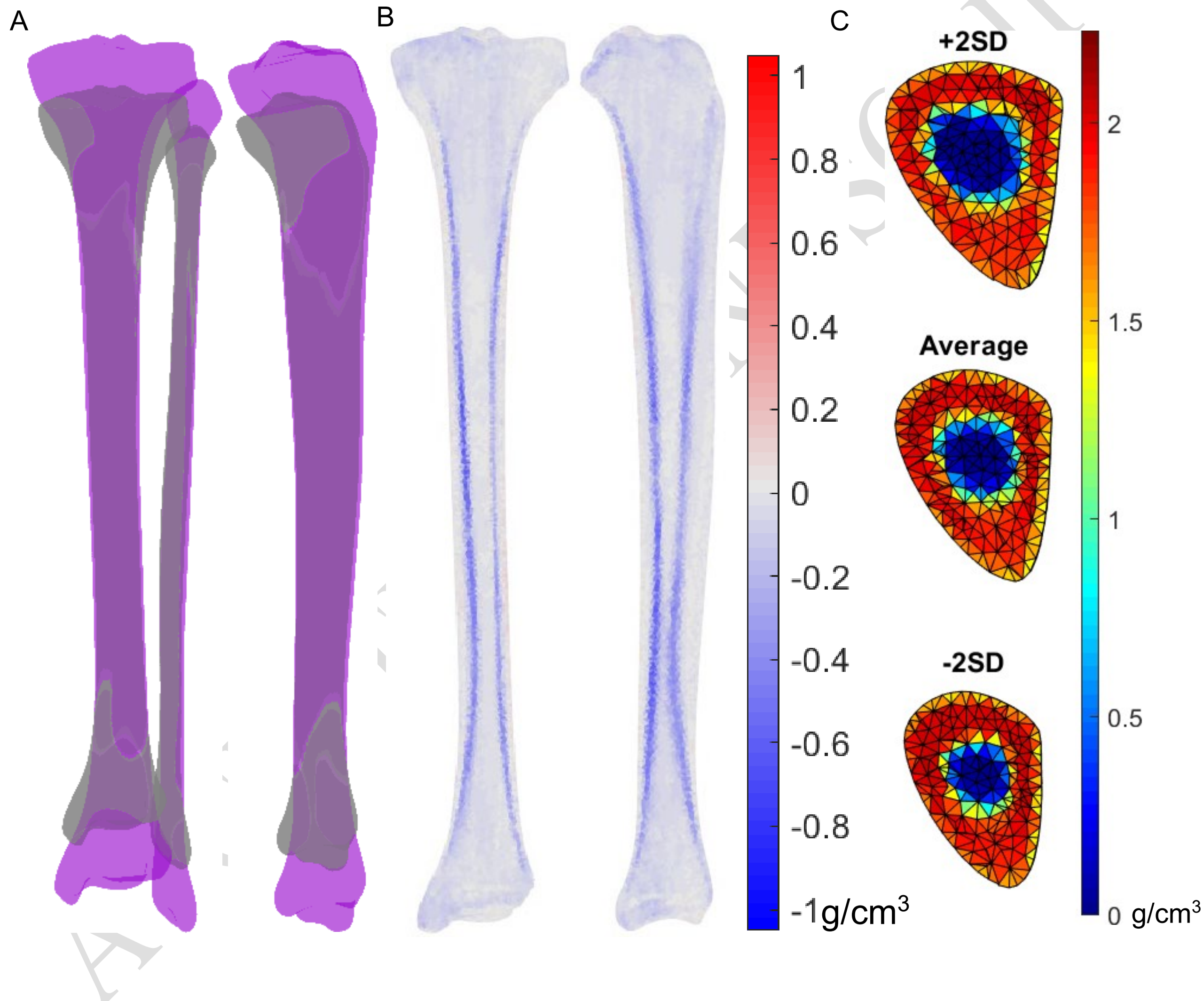

Figure S2: Geometry and density variations characterised by the second principal component (Presented in main article, Figure 1). Surface geometry of the tibia and fibula perturbed by +2 standard deviations (SD) (purple) and the average geometries (grey). (B) Frontal (left) and sagittal (right) cross-sections of the tibia illustrating differences in internal density distribution between +2 SD and average, where red indicates greater density in the model perturbed by +2 SD. (C) Axial cross-sections of the tibial diaphysis at 50% of total axial length.

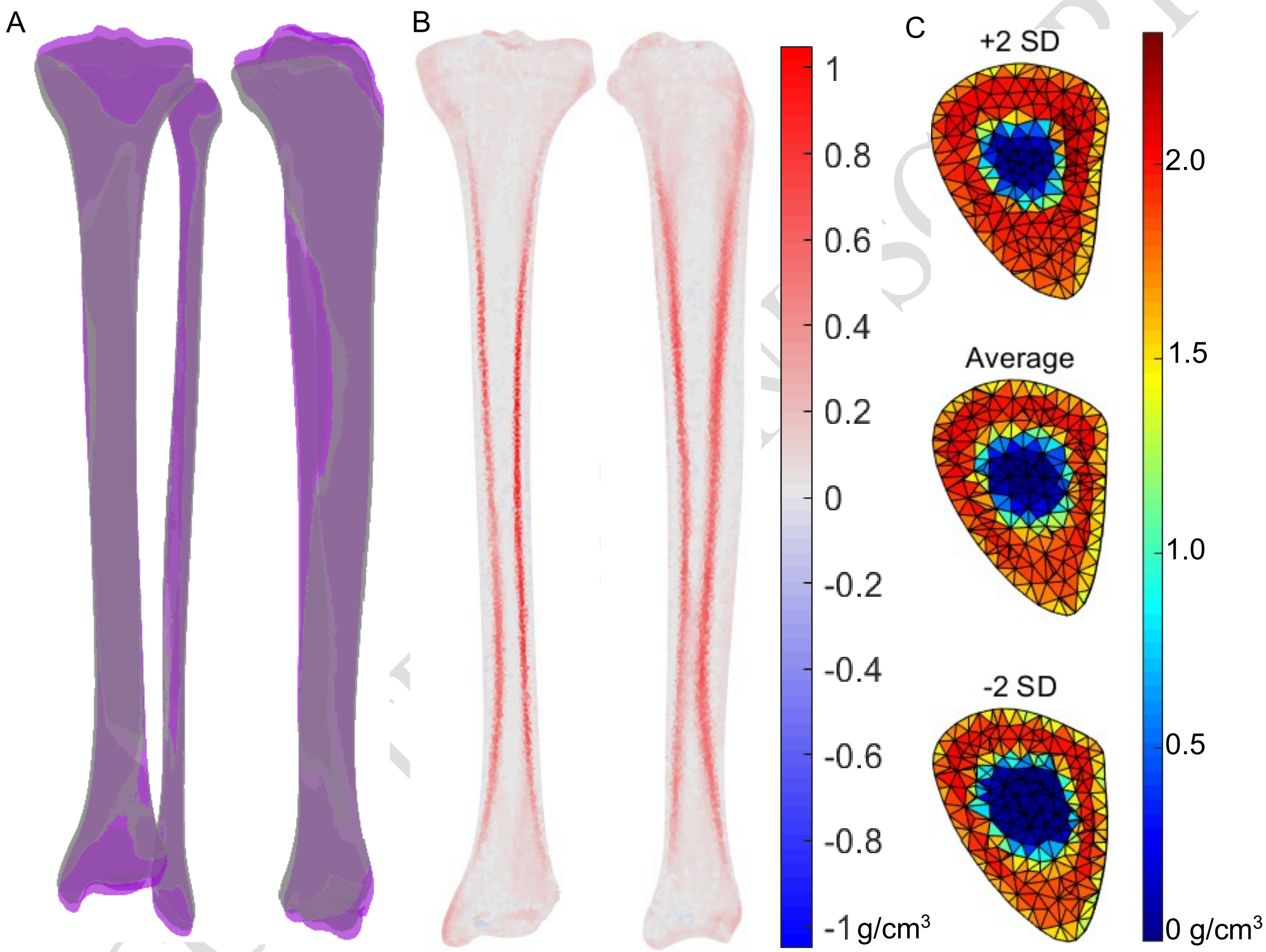

Figure S3: Geometry and density variations characterised by the third principal component. Surface geometry of the tibia and fibula perturbed by +2 standard deviations (SD) (purple) and the average geometries (grey). (B) Frontal (left) and sagittal (right) cross-sections of the tibia illustrating differences in internal density distribution between +2 SD and average, where red indicates greater density in the model perturbed by +2 SD. (C) Axial cross-sections of the tibial diaphysis at 50% of total axial length.

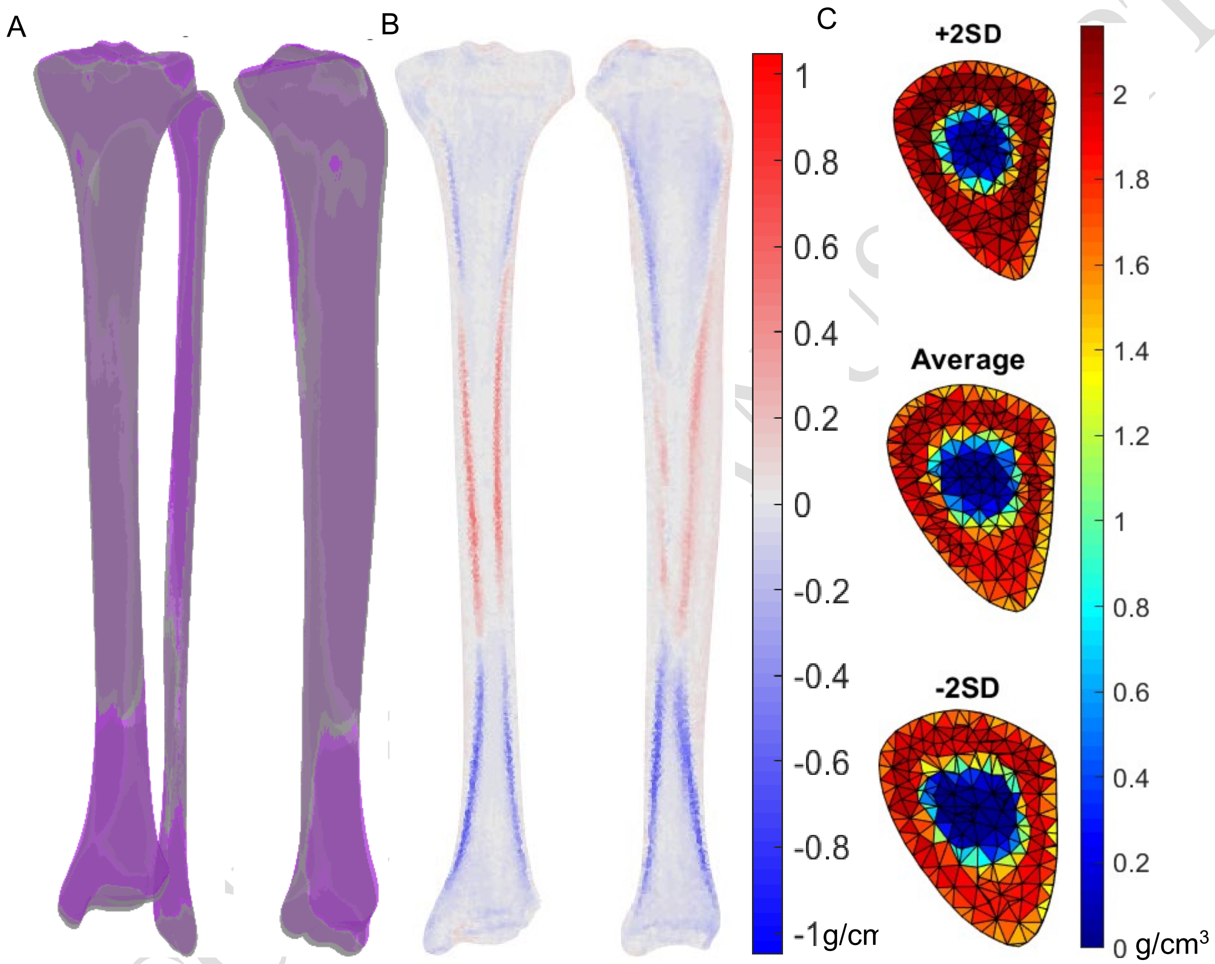

Figure S4: Geometry and density variations characterised by the fourth principal component. Surface geometry of the tibia and fibula perturbed by +2 standard deviations (SD) (purple) and the average geometries (grey). (B) Frontal (left) and sagittal (right) cross-sections of the tibia illustrating differences in internal density distribution between +2 SD and average, where red indicates greater density in the model perturbed by +2 SD. (C) Axial cross-sections of the tibial diaphysis at 50% of total axial length.

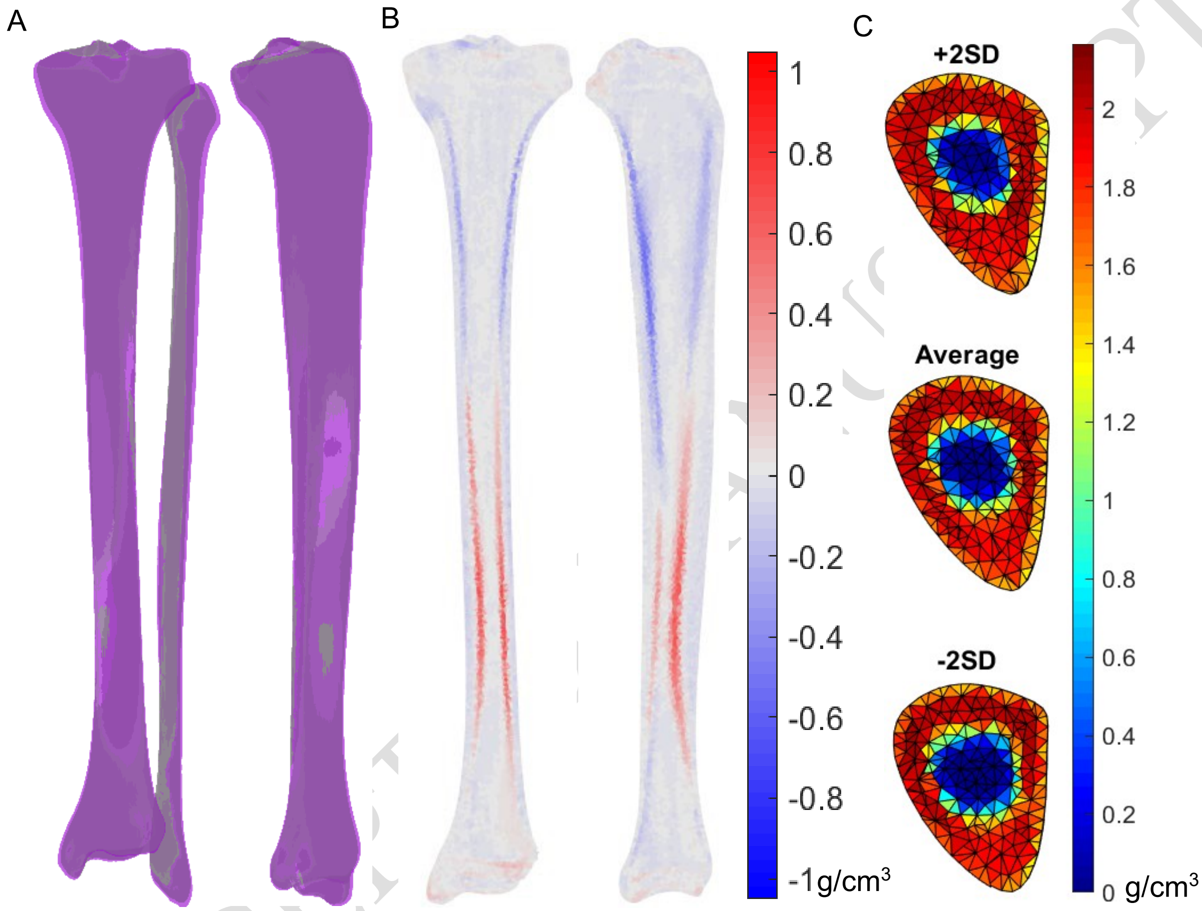

Figure S5: Geometry and density variations characterised by the fifth principal component. Surface geometry of the tibia and fibula perturbed by +2 standard deviations (SD) (purple) and the average geometries (grey). (B) Frontal (left) and sagittal (right) cross-sections of the tibia illustrating differences in internal density distribution between +2 SD and average, where red indicates greater density in the model perturbed by +2 SD. (C) Axial cross-sections of the tibial diaphysis at 50% of total axial length.

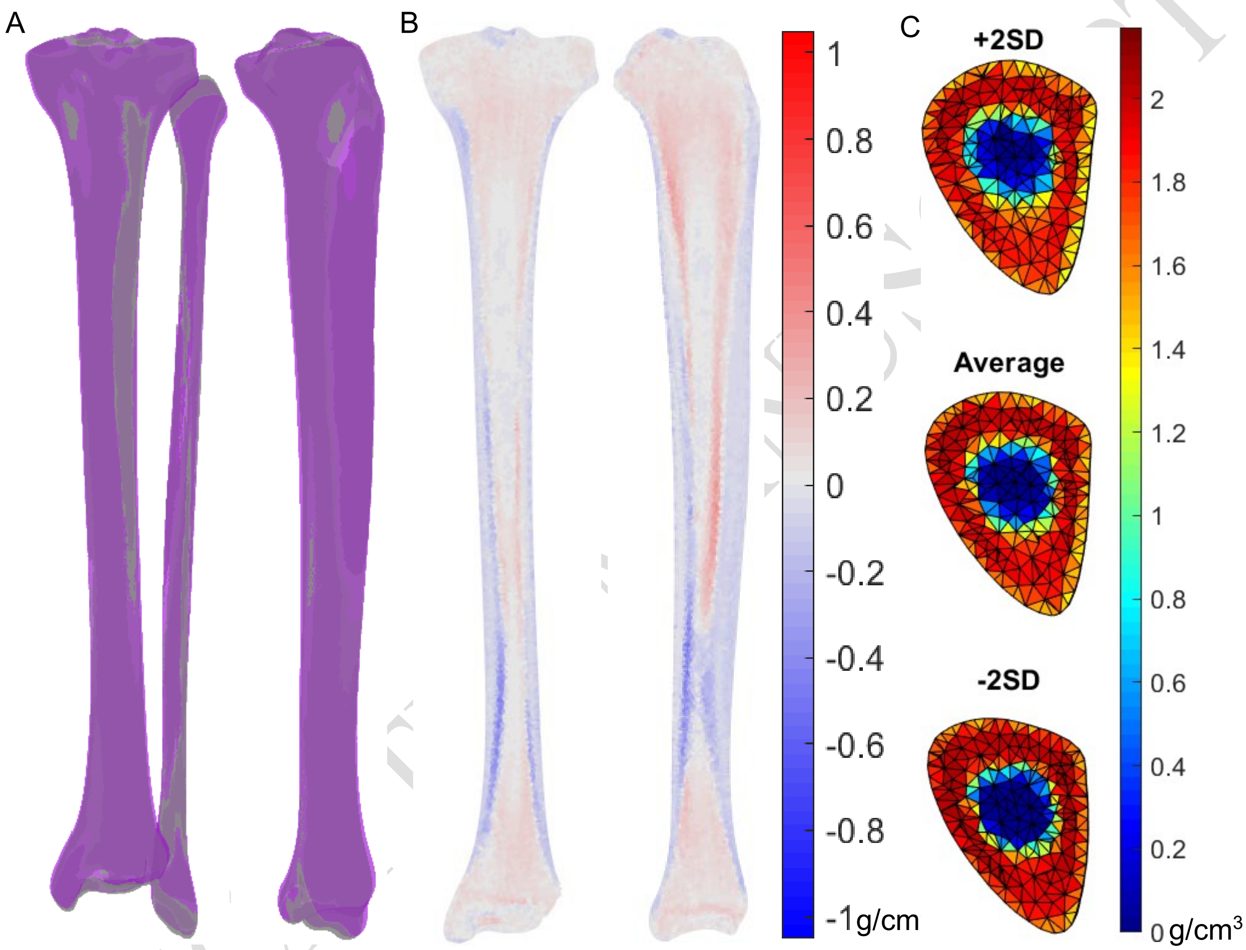

Figure S6: Mesh convergence analysis results. Blue dots show the peak strain (A) or strained volume (B) resulting from each mesh. Orange dots show the percentage change in peak strain or strained volume when compared to the previous (coarser) mesh. Strained volume resulting from the mesh with 42 413 elements was zero. As a result, the % change in strained volume between the 78 749 element mesh and the 42 413 element mesh was infinite and therefore not plotted.

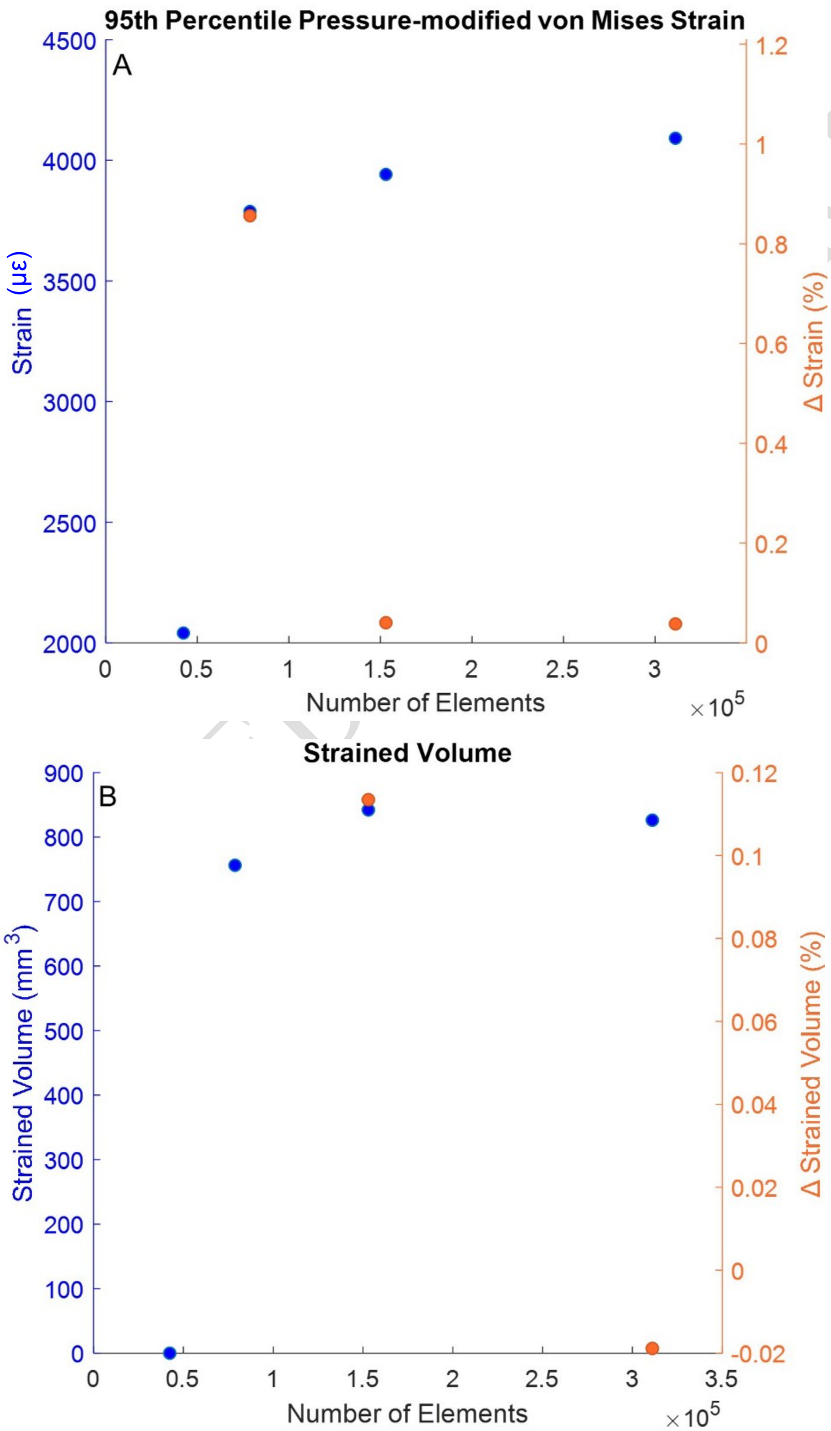

Table S1: Muscles included in the musculoskeletal model attaching to the tibia or fibula* and the forces applied to the finite element model, calculated from one female participant at the time of peak resultant ankle joint contact force. The ankle joint contact force applied at the ankle center of rotation is also shown. +: medial, anterior, proximal

Muscle	Muscle force applied to the tibia (N)		
	Medial/Lateral	Anterior/Posterior	Axial
Semimembranosus	-0.24	-2.16	2.14
Semitendinosus	0.22	-0.82	0.71
Biceps femoris long head	0.05	-0.69	0.69
Biceps femoris short head	-0.54	-6.17	11.48
Sartorius	24.03	-31.38	25.60
TFL	-32.83	-5.76	275.95
Gracilis	0.00	-0.36	0.49
Soleus	238.08	-272.39	-1930.42
Tibialis posterior	17.84	-5.28	-83.25
Flexor digitorum	4.28	-2.68	-27.56
Flexor hallucis	68.25	9.22	-242.60
Tibialis anterior	0.19	0.19	-1.19
Peroneus brevis	25.34	-20.92	-261.79
Peroneus longus	51.63	-25.42	-453.93
Peroneus tertius	0.99	2.00	-10.98
Extensor digitorum	2.29	2.01	-17.45
Extensor hallucis	0.79	0.96	-6.71
Patellar ligament	220.47	1679.08	3392.13
Ankle contact force	714.20	-1087.17	6241.07

* Mucles included in the musculoskeletal model that do not attach to the tibia or fibula were: gluteus maximus, gluteus medius, gluteus minimus, adductor longus, adductor brevis, adductor magnus, pectineus, iliacus, psoas, quadratus femoris, gemellus, piriformis, rectus femoris, vastus lateralis, vastus medialis, vastus intermedius, medial gastrocnemius, lateral gastrocnemius.

Musculoskeletal model:

E.M. Arnold, S.R. Ward, R.L. Lieber, S.L. Delp, A model of the lower limb for analysis of human movement, Ann. Biomed. Eng. (2010). https://doi.org/10.1007/s10439-009-9852-5.

Table S2: Muscle and joint contact forces applied to the tibia and fibula calculated from one male participant at the time of peak resultant ankle joint contact force. +: medial, anterior, proximal

Muscle	Muscle force applied to the tibia (N)		
	Medial/Lateral	Anterior/Posterior	Axial
Semimembranosus	1.03	-6.67	10.78
Semitendinosus	2.88	-5.35	3.96
Biceps femoris long head	2.65	-6.64	10.53
Biceps femoris short head	1.48	-4.63	13.25
Sartorius	6.46	-6.12	3.86
TFL	14.33	-47.43	169.35
Gracilis	0.66	-1.84	4.03
Soleus	-97.87	-207.19	-1664.85
Tibialis posterior	0.04	-0.27	-13.79
Flexor digitorum	-0.00	0.01	-0.04
Flexor hallucis	173.05	775.55	1881.25
Tibialis anterior	-0.13	-0.14	-2.46
Peroneus brevis	8.27	11.97	-144.89
Peroneus longus	-60.14	-27.05	-542.45
Peroneus tertius	-74.92	-18.52	-773.04
Extensor digitorum	-4.51	6.83	-31.85
Extensor hallucis	-9.19	14.22	-95.53
Patellar ligament	-0.88	1.33	-7.50
Ankle contact force	820.00	-952.08	6482.52